JMEPEG (2022) 31:8294–8303
https://doi.org/10.1007/s11665-022-06825-1

1059-9495/$19.00

TECHNICAL ARTICLE

Effect of Ti on the Microstructure and Mechanical Properties of AlCrFeNiTi$_x$ Eutectic High-Entropy Alloys

Songyuan Li, Feida Chen, Xiaobin Tang, Guojia Ge, Zhangjie Sun, Zhenlong Geng, Minyu Fan, and Ping Huang

Submitted: 8 September 2021 / Revised: 13 February 2022 / Accepted: 11 March 2022 / Published online: 31 March 2022

High-entropy alloys (HEAs) have become important candidates for structural materials of nuclear reactors because of their excellent mechanical properties and irradiation resistance. Recently, eutectic HEAs (EHEAs) have exhibited improved properties by double-phase strengthening. In this study, the effect of Ti on the microstructure and mechanical properties of the EHEAs AlCrFeNi was investigated. Results show that the eutectic microstructure consisted of a disordered body-center cubic (A2) phase and an ordered body-center cubic (B2) phase. Smaller nanoparticles were formed with Ti addition. Ti significantly influenced the microstructure of AlCrFeNi, thus changing the mechanical properties of AlCrFeNi. The compressive strength of AlCrFeNi increased, and the toughness of AlCrFeNi decreased with the increase in Ti content. The application of AlCrFeNiTi$_{0.2}$ alloy is promising because of its high mechanical properties and superior specific strength. In addition, the AlCrFeNiTi$_x$ alloys showed great softening resistance at a high temperature (500 °C).

Keywords eutectic high-entropy alloys, microstructure, mechanical properties, nanohardness

1. Introduction

Nuclear energy is critical for the future energy system due to its low carbon emission (Ref 1). Compared with the existing reactors, the Gen-IV reactors have high energy efficiency, low pollution, and a promising future (Ref 2). The structural materials for Gen-IV reactors endure high temperatures, high irradiation doses, and severe corrosion, resulting in significant volume swelling, segregation, and embrittlement of structural materials (Ref 3). Many investigations have devised new materials, such as high-entropy alloys (HEAs), oxide dispersion steel (ODS), and FeCrAl alloy (Ref 4-7), to meet the requirements of the Gen-IV reactors.

HEAs are multi-principal element alloys composed of five or more elements in an equal atomic ratio or nearly equal atomic ratio (Ref 8). Many studies have proven that HEAs have high strength, exceptional hardness at elevated temperatures, and excellent corrosion resistance (Ref 9-16). Furthermore, previous studies have emphasized that the HEAs have excellent irradiation resistance compared with conventional alloys owing to their unique lattice distortion effect. Therefore, HEAs are considered the important candidates for structural materials of nuclear reactors (Ref 17-19). Eutectic HEAs (EHEAs), as a special kind of HEAs, have low-energy phase boundary, high rupture strength, stable defect structure, and good high-temperature creep resistance (Ref 20-22). These features ensure the application of EHEAs in high-temperature environments (Ref 23, 24).

As one of the first known EHEA systems, Al-Co-Cr-Fe-Ni has outstanding strength and ductility (Ref 25, 26). Lu et al. (Ref 23) proposed AlCoCrFeNi$_{2.1}$, composed of alternating soft FCC and hard BCC phases, showing an unprecedented combination of high ductility and fracture strength. Lim et al. (Ref 27) studied the mechanical properties of AlCoCrFeNi at high temperatures. The alloy showed superior specific strength to TiAl and titanium alloys in the temperature range from 773 to 873 K. Composition optimization design is an effective way to enhance the microstructure and mechanical properties of the alloy. A large number of studies have focused on the addition of microalloying elements. Previous results (Ref 28) show that Ti has the following merits, including low density, high melting point, and large atomic radius, which can improve the mechanical properties of alloys. Chen et al. found Ti$_{0.15}$AlCoCrFeNi$_{2.1}$ alloys showed the most excellent combination of high ultimate tensile strength (1253 MPa) and ductility (12.9%) (Ref 28). Similarly, Munitz et al. added 11.1% Ti to AlCrFeNi to create AlCrFeNiTi$_{0.5}$, which increase the alloy strength from 1560 to 1660 MPa (Ref 29). Most recently, Elyorjon Jumaev et al. found the yield strength was improved from 1389 to 1703 MPa and high-temperature hardness was also enhanced after the addition of 5 at.% of Ti to AlCrFeNi (Ref 30). These researches suggest that the HEAs through Ti addition exhibit excellent performance. However, a systematic investigation of microstructure and mechanical properties of alloys caused by Ti addition is deficient. In addition, the element Co in the system has high neutron transmutation-induced radioactivity, which makes it unfavorable for nuclear applications. Thus, using Ti instead of Co to obtain high-performance

Songyuan Li, Feida Chen, Guojia Ge, Zhangjie Sun, and **Zhenlong Geng**, Department of Nuclear Science and Technology, Nanjing University of Aeronautics and Astronautics, Nanjing 211106, China; **Xiaobin Tang**, Department of Nuclear Science and Technology, Nanjing University of Aeronautics and Astronautics, Nanjing 211106, China; and Key Laboratory of Nuclear Technology Application and Radiation Protection in Astronautics, Ministry of Industry and Information Technology, Nanjing 211106, China; and **Minyu Fan** and **Ping Huang**, Suzhou Nuclear Power Research Institute, Suzhou 215004, China. Contact e-mail: fdchen@nuaa.edu.cn.

Al-Cr-Fe-Ni-Ti alloy and exploring the ideal content of Ti element are the cores of this study.

On the basis of the abovementioned discussion, AlCrFeNi-Ti_x (x=0, 0.2, 0.5, 1) alloys with different Ti contents were prepared. The effects of Ti content on the phase and microstructure of the material were systematically studied. The variations in compression strength and hardness under different Ti contents were also investigated.

2. Experimental

$AlCrFeNiTi_x$ (x=0, 0.2, 0.5, 1) alloys were prepared by cold crucible levitation melting under argon atmosphere, and they were denoted as "Ti0," "Ti0.2," "Ti0.5," and "Ti1" hereinafter. Before melting, the furnace was kept below the pressure of 7×10^{-3} Pa, and protective argon through the furnace was maintained under the constant pressure of 0.05 MPa. The purity of raw metals is higher than 99.95%. The ingots were slipped and remelted at least four times to ensure chemical homogeneity and finally became ingots with a mass of 200 g. The ingot was cut into $10 \times 10 \times 1$ mm^3 thin slices by wire-electrode cutting, abraded on SiC paper up to 2000 grit, and polished for subsequent characterization. Parts of the samples were subjected to heat treatment under a pressure of 1×10^{-4} Pa to investigate the softening resistance at a high temperature. To meet the requirement of sodium fast reactor (SFR), 500 °C was chosen as annealing temperature (Ref 31). The temperature increased from room temperature to 500 °C at a rate of 30 °C/min and reduced to 100 °C at a rate of 3 °C/min after being homogenized at 500 °C for 3.7 h.

Rigaku Ultima-IV x-ray diffraction (XRD) with Cu-Kα radiation was used to characterize the crystal structure and phase composition of the samples. The 2θ scanned from 20° to 100° with a speed of 5°/min. The microstructure was investigated by scanning electron microscope (SEM, TESCAN LYRA3) equipped with energy-dispersive spectrometry (EDS). The thermal behavior was analyzed by differential scanning calorimeter (DSC, NETZSCH STA 449F3) from room temperature to 1500 °C with a rate of 20 °C/min under Ar atmosphere. The microstructure and phase were characterized by transmission electron microscope (TEM, FEI Talos F200X). The TEM sample was prepared by mechanical polishing to about 60 μm thickness, followed by dual jet polishing in ethanol solution containing 9% $HClO_4$.

Cylinder specimens with 5 mm in diameter and 10 mm in height were prepared for compression tests. The tests were conducted at room temperature using WDW-100 with a strain rate of 1×10^{-3} s^{-1}. The Vickers hardness was tested under a load of 9.8 N for 10 s. In addition, the nano-indentation hardness of the samples was measured on Nano Indenter G200. The continuous stiffness measurement with a Berkovich-type indenter was adopted in the tests. The indentation depth of 1.7 μm and the interval of 34 μm were set for the sample. Each sample was tested five times to reduce errors.

3. Results and Discussion

3.1 Phases and Microstructure

Figure 1 shows the XRD patterns of as-cast $AlCrFeNiTi_x$ alloys. The phase without Ti addition is composed of disordered BCC (A2) and ordered BCC (B2). The overlapping diffraction peaks ((110), (211), (220)) of the BCC phase indicate that the lattice constants of A2 and B2 are similar. When the Ti content is less than 11 at.%, no diffraction peak of other phases in addition to the A2 and B2 is found. The diffraction peaks of A2 and B2 shift to the left slightly with Ti addition, indicating that the lattice constant increases after Ti addition. The lattice constants of the B2 phase are 2.909, 2.910, 2.952, and 2.930 Å for Ti0, Ti0.2, Ti0.5, and Ti1, respectively. The lattice constants of the A2 phase are 2.903, 2.899, 2.919, and 2.898 Å for the alloys. Ti1 also forms some intermetallic compounds, such as $L2_1$ phases. This finding is consistent with the results of previous studies (Ref 21).

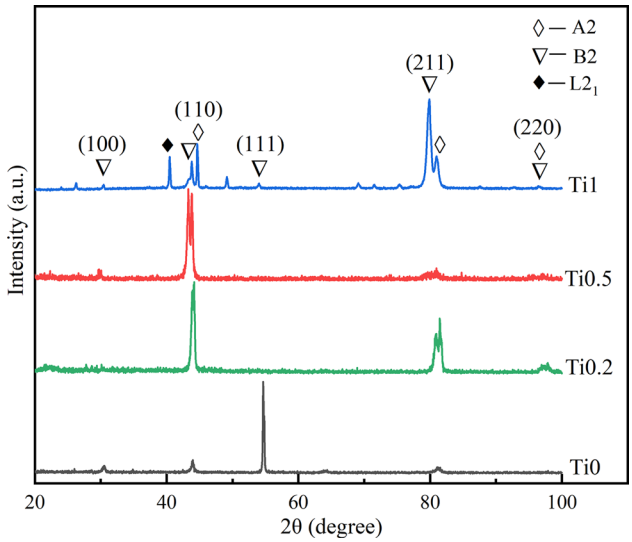

Fig. 1 XRD pattern of as-cast $AlCrFeNiTi_x$ alloys

The microstructures of $AlCrFeNiTi_x$ characterized by SEM are presented in Fig. 2. The four alloys have eutectic microstructures, which differ with different Ti additions. As presented in Fig. 2(a), the net-like eutectic microstructure occurs in Ti0. Each grain is composed of two regions: the core and the periphery. Two phases with different contrasts are observed in both regions. The high-magnification images in Fig. 2(b) show the periodic plate-like microstructure in the core, which is a typical feature of spinodal decomposition (Ref 32, 33). The morphology difference between the core region and the periphery is the least in Ti0 among all four alloys. The finer phase structure and more dense phase boundaries are formed in Ti0 than in other alloys. The ratio of the two phases is close to 1:1. As shown in Fig. 2(c), a typical net-like eutectic structure appears in Ti0.2, which gradually becomes larger from the central part to the periphery. In addition, the structure is composed of radiating lamellar phases, where nanometer-sized precipitates are distributed uniformly. The morphology of Ti0.5 (Fig. 2e) is similar to that of Ti0.2. The area of the phase with dark contrast in the periphery becomes larger, while the Ti element is added. Ti1 contains lamellar and cellular eutectic microstructure, and the lamellar thickness is less than 100 nm. In addition, the cellular microstructure is surrounded by fine lamellar microstructure. Figure 2(h) shows the enlarged morphology of the interface between the two kinds of eutectic microstructures. Nanoparticles marked with a yellow circle distribute uniformly in the center, and the size of nanoparticles was smaller than that of the particles in Ti0.5. Considering that

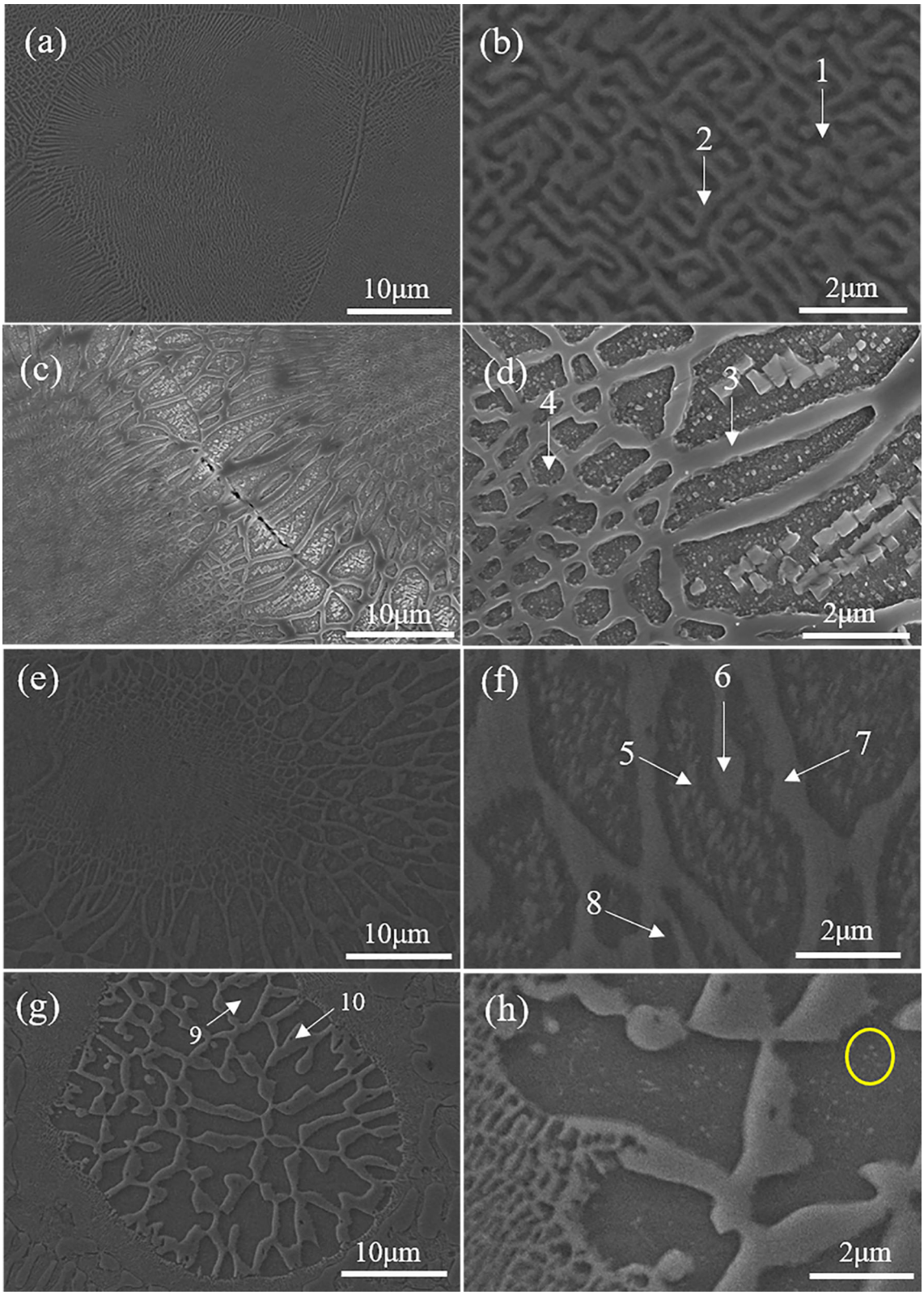

Fig. 2 SEM images of as-cast $AlCrFeNiTi_x$ alloys: (a) Ti0, (c) Ti0.2, (e) Ti0.5, (g) Ti1; (b), (d), (f), and (h) are the enlarged images of (a), (c), (e), and (g), respectively

Table 1 Chemical composition of the marked regions in Fig. 2 analyzed by EDS

Element	Al, at.%	Cr, at.%	Fe, at.%	Ni, at.%	Ti, at.%
Point 1	31.17 ± 1.6	18.83 ± 0.6	19.39 ± 0.8	30.62 ± 1.2	…
Point 2	12.12 ± 0.8	35.62 ± 1.2	36.34 ± 1.3	15.91 ± 0.8	…
Point 3	13.31 ± 0.7	36.33 ± 1.2	34.55 ± 1.3	13.19 ± 0.7	2.63 ± 0.2
Point 4	28.25 ± 2.1	22.19 ± 1.3	17.54 ± 1.2	23.87 ± 1.7	8.15 ± 0.7
Point 5	22.29 ± 1.3	16.62 ± 0.7	19.68 ± 0.8	27.07 ± 1.2	14.34 ± 0.5
Point 6	10.05 ± 0.6	47.56 ± 1.6	32.31 ± 1.2	5.58 ± 0.4	4.50 ± 0.2
Point 7	14.48 ± 0.7	43.36 ± 1.1	31.20 ± 1.0	5.99 ± 0.3	4.97 ± 0.2
Point 8	24.36 ± 1.2	10.28 ± 0.4	17.21 ± 0.6	30.53 ± 1.1	17.61 ± 0.6
Point 9	22.71 ± 1.4	11.47 ± 0.6	17.53 ± 0.9	26.29 ± 1.3	22.00 ± 0.9
Point10	13.57 ± 0.7	52.08 ± 1.6	19.68 ± 0.8	4.81 ± 0.3	9.86 ± 0.4

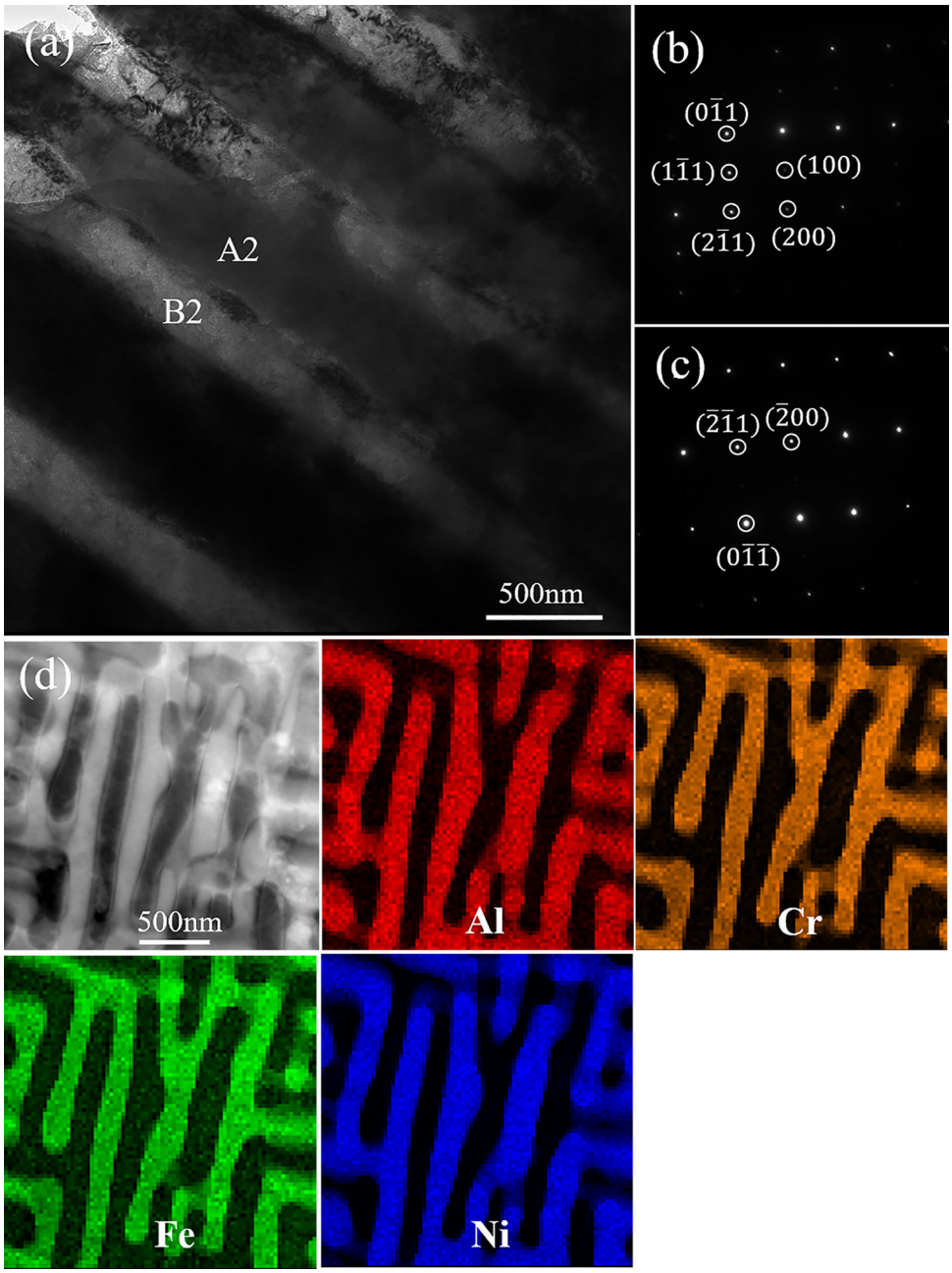

Fig. 3 TEM images and SAED patterns along [01 $\bar{1}$] zone axis of as-cast AlCrFeNi. (a) Bright-field image. (b) and (c) are the SAED patterns of bright and dark regions shown in (a), respectively. (d) shows EDS elemental mapping

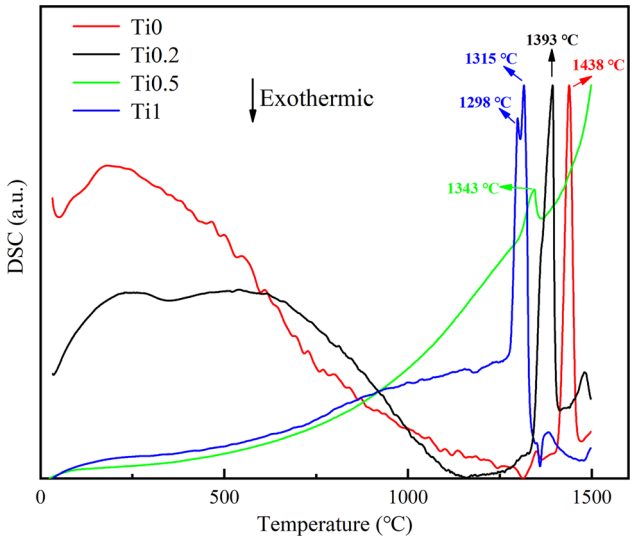

Fig. 4 Differential scanning calorimeter (DSC) curves for $AlCrFeNiTi_x$

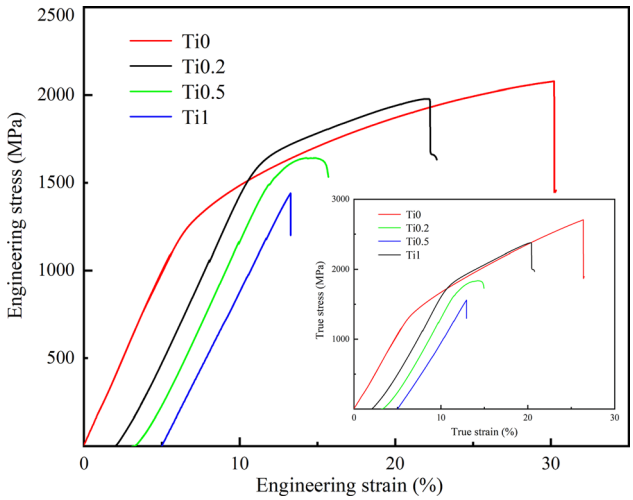

Fig. 5 Compression stress–strain curves of $AlCrFeNiTi_x$ at room temperature

the cooling rate can influence the microstructure during the solidification, we speculate Ti can influence the cooling rate. The microstructure morphology transforms from lamellae to petals with the addition of Ti, which is consistent with a previous study (Ref 28).

The chemical compositions of the marked regions in Fig. 2 are summarized in Table 1. In accordance with the chemical composition in Table 1, region 1 contains a large amount of Al and Ni, when region 2 contains a large amount of Fe and Cr. Based on previous studies, Ni-Al tends to form the B2 phase, while Fe-Cr tends to form the A2 phase (Ref 33, 34). Therefore, region 1 should be corresponding to B2 phase and region 2 should be corresponding to A2 phase. Furthermore, Ti segregates in the regions abundant in Ni, Al because of the negative enthalpy of mixing between Ti and Ni (Ref 35). EDS results confirm that regions 6, 7 are enriched in Cr and Fe, and regions 5, 8 are enriched in Al, Ni, and Ti. Therefore, regions 6, 7 are A2 phases, and regions 5, 8 are B2 phases. This finding is consistent with the XRD patterns.

AlCrFeNi was used to conduct the TEM characterization at the nanometer scale for further analyzing the eutectic microstructure, as shown in Fig. 3. The alloy shows an alternant structure with the bright and dark regions. The TEM sample has some corrosive area because of twin-jet electropolishing. The A2 and B2 phases show different corrosion resistances due to the different structures and chemical composition. The B2 phase has worse corrosion performance. The diffraction pattern of the bright region is presented in Fig. 3(b), and that of the dark region is presented in Fig. 3(c). The bright region is B2 due to the superlattice spots presented in Fig. 3(b). Referring to the results of EDS mapping, B2 is NiAl phase, while A2 is CrFe phase. The width of B2 is approximately 200 nm, while A2 is nearly 400 nm.

3.2 Differential Scanning Calorimeter (DSC)

DSC tests were conducted on the samples to determine the change in eutectic temperature of four alloys with different Ti contents. Figure 4 shows the DSC curves of different samples heated from room temperature to 1500 °C. The peak in the curves corresponds to the melting endothermic reaction of the materials. Ti0, Ti0.2, and Ti0.5 have an obvious endothermic peak at 1438, 1393, and 1343 °C, respectively. No other peak is found elsewhere, which means that the alloys are eutectic. By contrast, Ti1 has the main peak at 1315 °C and a small peak at 1298 °C. Therefore, the melting point of these intermetallic

Table 2 Compressive mechanical properties of $AlCrFeNiTi_x$ at room temperature

Alloy	Yield Strength, MPa	Fracture Strength, MPa	Strain, %	Density, g/cm^3	Specific YS, MPa·cm^3/g
AlCrFeNi	1167.45	2077.54	30.21	6.64±0.04	175.83
$AlCrFeNiTi_{0.2}$	1556.88	1977.93	18.46	6.55±0.03	237.80
$AlCrFeNiTi_{0.5}$	1488.21	1641.30	11.32	6.42±0.05	231.90
AlCrFeNiTi	1416.45	1440.43	8.28	6.22±0.03	227.62

Table 3 Compressive properties of some typical HEAs at room temperature

Alloy	Yield Strength, MPa	Fracture Strength, MPa	Strain, %	Ref.
AlCoCrFeNi	1313.7	1943.2	19	(Ref 25)
Al0.6CoCrFeNi	~400	~1400	78	(Ref 36)
CoCrFeNiV	1435	1665	2.5	(Ref 37)
CoCrFeNiMnV	1660	1845	0.5	(Ref 37)
VNbMoTaW	1246	1087	17	(Ref 38)

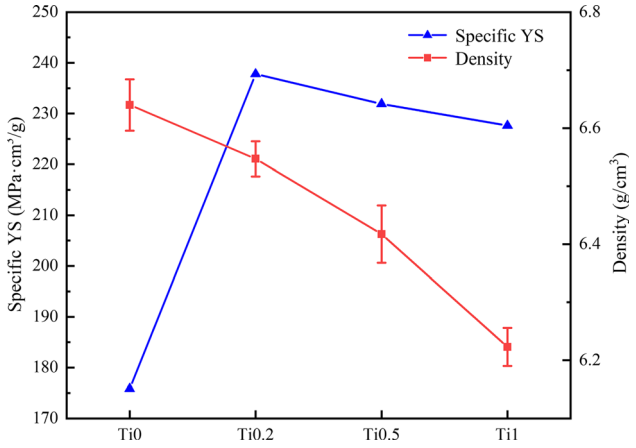

Fig. 6 Density and specific yield strength of $AlCrFeNiTi_x$

compounds is similar to the temperature of the eutectic reaction. With the addition of Ti, the melting temperature (T_m) tends to diminish, which will be favorable for castability.

3.3 Mechanical Properties

Engineering compressive stress–strain curves for as-cast $AlCrFeNiTi_x$ alloy are presented in Fig. 5, and the results are summarized in Table 2. The figure inset shows the true stress–strain curve of the samples. Table 3 shows the mechanical properties of some typical HEAs reported in the literature. The noticeable effect of Ti addition can be confirmed on the compressive behavior of the alloys. Increasing Ti content from 0 to 0.2 increases yield strength from 1167 to 1556 MPa. However, the addition of Ti decreases fracture strength from 2077 to 1977 MPa. At the same time, the maximum strain decreases from 30.21 to 18.46%. Owing to the uniform microstructure, Ti0 can distribute the deformation and stress concentration more uniformly, which can suffer much more deformation without cracking and breakage.

The atomic radius of Ti is relatively large. The lattice distortion can be expressed in the difference of atomic size (δ).

$$\delta = \sqrt{\sum_{i=1}^{n} c_i (1 - r_i/\bar{r})^2} \qquad \text{(Eq 1)}$$

where c_i and r_i are the atom fraction and radius of element i, respectively. $\bar{r}$ is the average radius of the elements in the alloys.

To measure the lattice distortion of the alloys, we calculate the parameters of the two phases. The parameter in AlCrFeNi is 5.60% for A2 phase, and 6.25% for B2 phase. After the addition of Ti, the parameter of atomic size mismatch for both of the two phases increases insignificantly. The parameter in $AlCrFeNiTi_{0.2}$ is 5.64% for A2 phase, and 6.44% for B2 phase. Based on the parameter of atomic size mismatch, we can deduce that the main reason for the increased strength in Ti0.2 is not the enhancement of lattice distortion. In the other hand, the dispersed nanoparticles in the matrix for Ti0.2 may also inhibit the migration of dislocation to increase the strength. And Ti content also affects the growth of microstructure, which increase the volume fraction of B2 phase. B2 phase has higher strength than A2 phase in general. Therefore, the addition of Ti reduces the plasticity and toughness of $AlCrFeNiTi_x$ alloys and decreases the fracture strength and strain of $AlCrFeNiTi_x$ alloys. In addition to the three factors above, brittle phase-$L2_1$ phase formed in Ti1 can result in the drop of toughness. Specific yield strength is an important index for alloys, and it is summarized in Fig. 6. As the Ti content increases, the density of the material decreases, and the specific yield strength increases constantly. The specific yield strength of all the four materials is higher than 175 $MPa{\cdot}cm^3/g$. The proposed $AlCrFeNiTi_{0.2}$ shows superior specific yield strength at room temperature.

The fracture surface of $AlCrFeNiTi_x$ was characterized by SEM, as shown in Fig. 7. Figure 7(a) shows that the fracture surface of Ti0 is relatively rough. Slip separation is observed in Fig. 7(b), and it is one of the features of plastic fracture. The trench-like microstructure appears in Ti0.2 due to different deformation behaviors of A2 and B2. The fracture pattern belongs to ductile fracture as the dimples observed in Ti0.2. River-like patterns and tearing edges for Ti0.5 can be observed in Fig. 7(f). Cleavage steps and obvious grain boundaries indicate that the material has a quasi-cleavage fracture, which is the reason for the sharp decrease in the strain of the material. The fracture surface of Ti1 in Fig. 7(g) is smooth with some cracks. A large number of tearing edges indicate that the material has undergone a cleavage fracture.

3.4 Microhardness

The mechanical properties are determined by microstructure, which can be significantly affected by temperature. When the material is subjected to high-temperature environments, the decrease in material hardness may cause failure. Thus, softening resistance is important for structural materials applied in nuclear reactors. The hardness of the as-cast and annealed samples was characterized to test the softening resistance of the material at an elevated temperature. We list the average Vickers hardness taken from ten indents in Table 4. The average Vickers hardness values for as-cast Ti0, Ti0.2, Ti0.5, and Ti1 samples are 409 ± 4, 499 ± 4, 549 ± 8 and 567 ± 9 HV, respectively. And the hardness of the samples did not change significantly after the heat treatment.

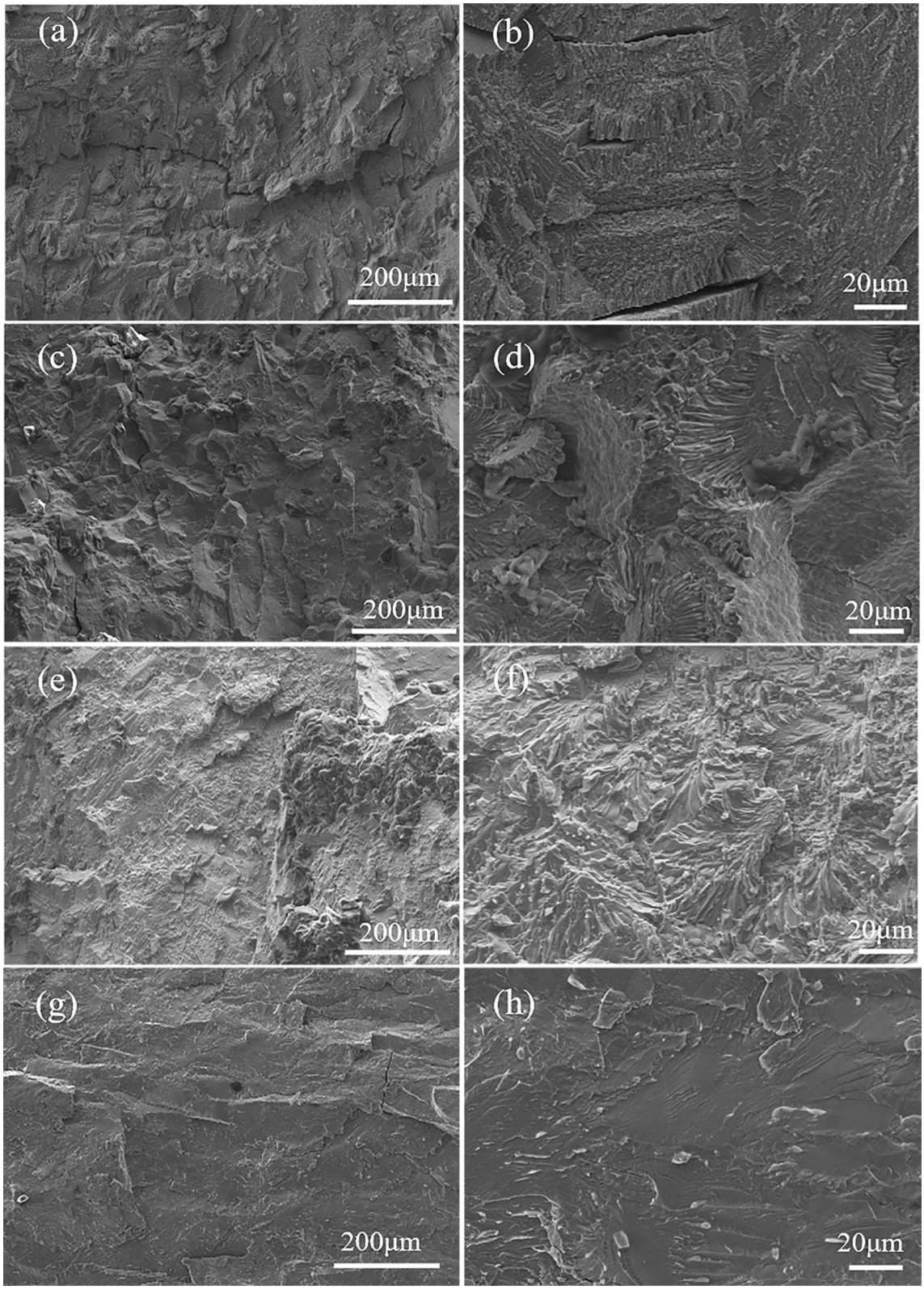

Fig. 7 SEM images of fracture surface of $AlCrFeNiTi_x$: (a) x= 0, (c) x = 0.2, (e) x = 0.5, (g) x = 1; (b), (d), (f), and (h) are the enlarged images of (a), (c), (e), and (g), respectively

Nano-indentation is also used to measure hardness, and Nix–Gao model is used to characterize the change in material hardness with depth (Ref 39). The model fitting formula is given as follows:

$$H = H_0 \sqrt{1 + \frac{h^*}{h}} \quad \text{(Eq 2)}$$

where H is the hardness, H_0 is the hardness in the limit of infinite depth, h^* is the characteristic length determined by the shape of an indenter and the material, and h is the indentation depth of the material. The hardness values are inaccurate when the indented depth is less than dozens of nanometers because of the reverse indentation size effect (RISE). The hardness corresponding to a depth of less than 150 nm is discarded due to the surface effect. Figure 8(a) shows the relationship between hardness and depth, and Figure 8(b) presents the relationship between the reciprocal of the depth (h^{-1}) and the square of the hardness (H^2). As shown in Fig. 8(b), the curves of Ti0 have inflection points when the depth is around 500 nm. This result indicates that the surface hardness is different from the matrix hardness of the material. According to previous reports (Ref 23, 40), the EHEAs may have a large strain hardening phenomenon because of regular structure that easily stores dislocations and alternating phases. The material needs to be abraded and polished before testing, forming a hardening layer of hundreds of nanometers. Therefore, hardness varies from the surface toward the core. The nanohardness of the material is summarized in Table 4. The hardness is 5.19 GPa without Ti addition. By contrast, the hardness increases significantly after Ti addition, and it is higher than 7 GPa, maybe because Ti promotes the lattice distortion of the alloy and intermetallic compounds form in Ti1. However, the hardness of the material does not change significantly after the high-temperature treatment at 500 °C. This finding means that the material has good softening resistance at a high temperature.

Table 4 Vickers Hardness and nanohardness results of as-cast and annealed AlCrFeNiTi$_x$

Alloy	Nanohardness, GPa	Vickers Hardness, HV
Ti0 (as-cast)	5.19 ± 0.16	409 ± 4
Ti0 (annealed)	5.29 ± 0.68	411 ± 7
Ti0.2 (as-cast)	6.86 ± 0.22	499 ± 4
Ti0.2 (annealed)	7.26 ± 0.23	526 ± 9
Ti0.5 (as-cast)	7.10 ± 0.27	549 ± 8
Ti0.5 (annealed)	7.28 ± 0.20	550 ± 3
Ti1 (as-cast)	7.69 ± 0.45	567 ± 9
Ti1 (annealed)	8.02 ± 0.29	570 ± 4

4. Summary

In this study, AlCrFeNiTi$_x$ (x=0, 0.2, 0.5, 1) was synthesized by cold crucible levitation melting. The effect of Ti content on the phase structure, microstructure, and mechanical properties of AlCrFeNiTi$_x$ was analyzed systematically. The major conclusions of this study are drawn as follows:

1. The XRD showed ordered BCC and disordered BCC in the three types of alloys. Furthermore, $L2_1$ phases were formed in Ti1. The feature of the eutectic structure was found from SEM images, which was identified to be the combination of the B2 phase (Ni, Al) and the A2 phase (Fe, Cr). Nanosized precipitates could be observed inside the B2 phase with the Ti addition.
2. With the addition of Ti, the yield strength of AlCrFeNiTi$_x$ alloys increased from 1167 MPa (Ti0) to 1556 MPa (Ti0.2). However, the toughness of AlCrFeNiTi$_x$ alloys decreased at the same time. Due to the low density of alloys (<7 g/cm^3), alloys can be defined as lightweight alloys. The addition of Ti decreased the density and increased the specific yield strength of AlCrFeNiTi$_x$ alloys. The specific yield strength of Ti0.2 even reached 237 MPa·cm^3/g.
3. The hardness of the alloys increased with Ti addition. After high-temperature annealing, the hardness of AlCrFeNiTi$_x$ alloys changed insignificantly, which meant that the material had great softening resistance at a high temperature (500 °C).

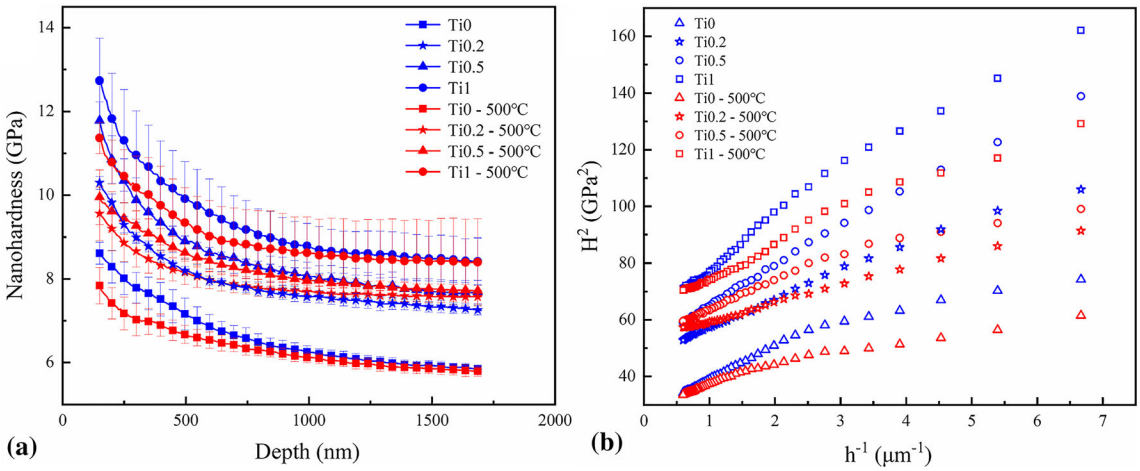

Fig. 8 (a) Average nanohardness versus the indentation depth of as-cast and annealed AlCrFeNiTi$_x$; (b) Curves of H^2-h^{-1} for average nanohardness of the alloy

Acknowledgments

This work was supported by China Postdoctoral Science Foundation (Grant No. 2020M671488), the Fundamental Research Funds for the Central Universities (Grant No. NS2021036), Jiangsu Planned Projects for Postdoctoral Research Funds (Grant No. 2021K222B), the Postgraduate Research & Practice Innovation Program of Jiangsu Province (Grant No. KYCX20_0196).

References

1. S. Chu and A. Majumdar, Opportunities and Challenges for a Sustainable Energy Future, *Nature*, 2012, **488**(7411), p 294–303
2. U.S. Doe, "A Technology Roadmap for Generation IV Nuclear Energy Systems," 2002
3. S.J. Zinkle and G. Was, Materials Challenges in Nuclear Energy, *Acta Mater.*, 2013, **61**(3), p 735–758
4. S.Q. Xia, X. Yang, T.F. Yang, S. Liu and Y. Zhang, Irradiation Resistance in AlxCoCrFeNi High Entropy Alloys, *JOM*, 2015, **67**(10), p 2340–2344
5. P. Song, D. Morrall, Z. Zhang, K. Yabuuchi and A. Kimura, Radiation Response of ODS Ferritic Steels with Different Oxide Particles Under Ion-Irradiation at 550 °C, *J. Nucl. Mater.*, 2018, **502**, p 76–85
6. P. Jin, T. Shen, M. Cui, Y. Zhu, B. Li, T. Zhang, J. Li, S. Jin, E. Lu, X. Cao and Z. Wang, Study on Vacancy-type Defects in SIMP Steel Induced by Separate and Sequential H and He Ion Implantation, *J. Nucl. Mater.*, 2019, **520**, p 131–139
7. V. Shivam, J. Basu, V.K. Pandey, Y. Shadangi and N.K. Mukhopadhyay, Alloying Behaviour, Thermal Stability and Phase Evolution in Quinary AlCoCrFeNi High Entropy Alloy, *Adv. Powder Technol.*, 2018, **29**(9), p 2221–2230
8. J.W. Yeh, S.K. Chen, S.J. Lin, J.Y. Gan, T.S. Chin, T.T. Shun, C.H. Tsau and S.Y. Chang, Nanostructured High-Entropy Alloys with Multiple Principal Elements: Novel Alloy Design Concepts and Outcomes, *Adv. Eng. Mater.*, 2004, **6**(5), p 299–303
9. C.W. Tsai, M.H. Tsai, J.W. Yeh and C.C. Yang, Effect of Temperature on Mechanical Properties of Al0.5CoCrCuFeNi Wrought Alloy, *J. Alloys Compd.*, 2010, **490**(1), p 160–165
10. T. Shi, P.H. Lei, X. Yan, J. Li, Y.D. Zhou, Y.P. Wang, Z.X. Su, Y.K. Dou, X.F. He, D. Yun, W. Yang and C.Y. Lu, Current Development of Body-Centered Cubic High-Entropy Alloys for Nuclear Applications, *Tungsten*, 2021, **3**(2), p 197–217
11. Z. Jiang, W. Chen, Z. Xia, W. Xiong and Z. Fu, Influence of Synthesis Method on Microstructure and Mechanical Behavior of Co-free AlCrFeNi Medium-Entropy Alloy, *Intermetallics*, 2019, **108**, p 45–54
12. M. Shabani, J. Indeck, K. Hazeli, P.D. Jablonski and G.J. Pataky, Effect of Strain Rate on the Tensile Behavior of CoCrFeNi and CoCrFeMnNi High-Entropy Alloys, *J. Mater. Eng. Perform.*, 2019, **28**(7), p 4348–4356
13. H.A. Aly, K.A. Abdelghafar, G.A. Gaber and L.Z. Mohamed, Fabrication, Characterization, and Corrosion Behavior of a New Cu40Mn25Al20Fe5Co5Ni5 High-Entropy Alloy in HNO3 Solution, *J. Mater. Eng. Perform.*, 2021, **30**(2), p 1430–1443
14. M. Wang, H. Cui, Y. Zhao, C. Wang, N. Wei, Y. Zhao, X. Zhang and Q. Song, A Simple Strategy for Fabrication of an FCC-based Complex Concentrated Alloy Coating with Hierarchical Nanoprecipitates and Enhanced Mechanical Properties, *Mater. Design*, 2019, **180**, p 107893
15. Y. Lu, H. Huang, X. Gao, C. Ren, J. Gao, H. Zhang, S. Zheng, Q. Jin, Y. Zhao, C. Lu, T. Wang and T. Li, A Promising New Class of Irradiation Tolerant Materials: Ti2ZrHfV0.5Mo0.2 High-Entropy Alloy, *J. Mater. Sci. Technol.*, 2019, **35**(3), p 369–373
16. M. Wang, Y. Lu, G. Zhang, H. Cui, D. Xu, N. Wei and T. Li, A Novel High-Entropy Alloy Composite Coating with Core-Shell Structures Prepared by Plasma Cladding, *Vacuum*, 2021, **184**, p 109905
17. C. Lu, T. Yang, K. Jin, N. Gao, P. Xiu, Y. Zhang, F. Gao, H. Bei, W.J. Weber, K. Sun, Y. Dong and L. Wang, Radiation-Induced Segregation on Defect Clusters in Single-Phase Concentrated Solid-Solution Alloys, *Acta Mater.*, 2017, **127**, p 98–107
18. S. Xia, M.C. Gao, T. Yang, P.K. Liaw and Y. Zhang, Phase Stability and Microstructures of High Entropy Alloys Ion Irradiated to High Doses, *J. Nucl. Mater.*, 2016, **480**, p 100–108
19. S. Shen, F. Chen, X. Tang, G. Ge, J. Gao and Z. Sun, Irradiation Damage and Swelling of Carbon-Doped Fe38Mn40Ni11Al4Cr7 High-Entropy Alloys Under Heavy Ion Irradiation at Elevated Temperature, *J. Mater. Sci.*, 2020, **55**(36), p 17218–17231
20. Y. Lu, X. Gao, L. Jiang, Z. Chen, T. Wang, J. Jie, H. Kang, Y. Zhang, S. Guo, H. Ruan, Y. Zhao, Z. Cao and T. Li, Directly Cast Bulk Eutectic and Near-Eutectic High Entropy Alloys with Balanced Strength and Ductility in a Wide Temperature Range, *Acta Mater.*, 2017, **124**, p 143–150
21. M. Wang, Y. Lu, T. Wang, C. Zhang, Z. Cao, T. Li and P.K. Liaw, A Novel Bulk Eutectic High-Entropy Alloy with Outstanding As-cast Specific Yield Strengths at Elevated Temperatures, *Scripta Mater*, 2021, **204**, p 114132
22. Y. Lu, Y. Dong, H. Jiang, Z. Wang, Z. Cao, S. Guo, T. Wang, T. Li and P.K. Liaw, Promising Properties and Future Trend of Eutectic High Entropy Alloys, *Scripta Mater.*, 2020, **187**, p 202–209
23. Y. Lu, Y. Dong, S. Guo, L. Jiang, H. Kang, T. Wang, B. Wen, Z. Wang, J. Jie, Z. Cao, H. Ruan and T. Li, A Promising New Class of High-Temperature Alloys: Eutectic High-Entropy Alloys, *Sci Rep*, 2014, **4**, p 6200
24. S. Wolff-Goodrich, A. Marshal, K.G. Pradeep, G. Dehm, J.M. Schneider and C.H. Liebscher, Combinatorial Exploration of B2/L21 Precipitation Strengthened AlCrFeNiTi Compositionally Complex Alloys, *J. Alloys Compd.*, 2021, **853**, p 156111
25. M. Kang, K.R. Lim, J.W. Won and Y.S. Na, Effect of Co Content on the Mechanical Properties of A2 and B2 Phases in AlCoxCrFeNi High-Entropy Alloys, *J. Alloys Compd.*, 2018, **769**, p 808–812
26. L. Meshi, Y. Linden, A. Munitz, S. Salhov and M. Pinkas, Retardation of the σ Phase Formation in the AlCoCrFeNi Multi-Component Alloy, *Mater. Charact.*, 2019, **148**, p 171–177
27. K.R. Lim, K.S. Lee, J.S. Lee, J.Y. Kim, H.J. Chang and Y.S. Na, Dual-Phase High-Entropy Alloys for High-Temperature Structural Applications, *J. Alloys Compd.*, 2017, **728**, p 1235–1238
28. X. Chen, W. Xie, J. Zhu, Z. Wang, Y. Wang, Y. Ma, M. Yang, W. Jiang, H. Yu, Y. Wu and X. Hui, Influences of Ti Additions on the Microstructure and Tensile Properties of AlCoCrFeNi2.1 Eutectic High Entropy Alloy, *Intermetallics*, 2021, **128**, p 107024
29. A. Munitz, S. Salhov, G. Guttmann, N. Derimow and M. Nahmany, Heat Treatment Influence on the Microstructure and Mechanical Properties of AlCrFeNiTi0 5 High Entropy Alloys, *Mater. Sci. Eng. A*, 2019, **742**, p 1–14
30. E. Jumaev, M.A. Abbas, S.C. Mun, G. Song, S.-J. Hong and K.B. Kim, Nano-Scale Structural Evolution of Quaternary AlCrFeNi Based High Entropy Alloys by the Addition of Specific Minor Elements and its Effect on Mechanical Characteristics, *J. Alloys Compd.*, 2021, **868**, p 159217
31. G.S. Was, D. Petti, S. Ukai and S. Zinkle, Materials for Future Nuclear Energy Systems, *J. Nucl. Mater.*, 2019, **527**, p 151837
32. L.J. Santodonato, Y. Zhang, M. Feygenson, C.M. Parish, M.C. Gao, R.J. Weber, J.C. Neuefeind, Z. Tang and P.K. Liaw, Deviation from High-Entropy Configurations in the Atomic Distributions of a Multi-Principal-Element Alloy, *Nat. Commun.*, 2015, **6**, p 5964
33. S. Singh, N. Wanderka, B.S. Murty, U. Glatzel and J. Banhart, Decomposition in Multi-Component AlCoCrCuFeNi High-Entropy Alloy, *Acta Mater.*, 2011, **59**(1), p 182–190
34. X. Chen, J.Q. Qi, Y.W. Sui, Y.Z. He, F.X. Wei, Q.K. Meng and Z. Sun, Effects of Aluminum on Microstructure and Compressive Properties of Al-Cr-Fe-Ni Eutectic Multi-Component Alloys, *Mater. Sci. Eng. A*, 2017, **681**, p 25–31
35. A. Takeuchi and A. Inoue, Classification of Bulk Metallic Glasses by Atomic Size Difference, Heat of Mixing and Period of Constituent Elements and Its Application to Characterization of the Main Alloying Element, *Mater. Trans*, 2005, **46**(12), p 2817–2829
36. J. Joseph, T. Jarvis, X. Wu, N. Stanford, P. Hodgson and D.M. Fabijanic, Comparative Study of the Microstructures and Mechanical Properties of Direct Laser Fabricated and Arc-Melted AlxCoCrFeNi High Entropy alloys, *Mater. Sci. Eng., A*, 2015, **633**, p 184–193
37. G.A. Salishchev, M.A. Tikhonovsky, D.G. Shaysultanov, N.D. Stepanov, A.V. Kuznetsov, I.V. Kolodiy, A.S. Tortika and O.N. Senkov, Effect of Mn and V on Structure and Mechanical Properties of High-Entropy Alloys Based on CoCrFeNi System, *J. Alloys Compd.*, 2014, **591**, p 11–21
38. O.N. Senkov, G.B. Wilks, J.M. Scott and D.B. Miracle, Mechanical Properties of Nb25Mo25Ta25W25 and V20Nb20Mo20Ta20W20

Refractory High Entropy Alloys, *Intermetallics*, 2011, **19**(5), p 698–706
39. W.D. Nix and H. Gao, Indentation Size Effects in Crystalline Materials: A Law for Strain Gradient Plasticity, *J. Mech. Phys. Solids*, 1998, **46**(3), p 411–425
40. S. Liu, M.C. Gao, P.K. Liaw and Y. Zhang, Microstructures and Mechanical Properties of Al CrFeNiTi0.25 Alloys, *J. Alloys Compd*, 2015, **619**, p 610–615